(Received 12 March 2026, Accepted 7 April 2026, Scheduled 29 April 2026)

Optimal Control of Electromagnetic Performance for PMSM Dual-Loop System Based on Improved Fuzzy NLADRC

Dehai Chen[1,2], Haifeng Zhang[1,*], Ruilong Liu[1], and Lingfeng Cai[1]

[1] School of Electrical Engineering and Automation, Jiangxi University of Science and Technology, Ganzhou 341000, Jiangxi, China
[2] Ganjiang Innovation Academy, Chinese Academy of Sciences, Ganzhou 341000, Jiangxi, China

ABSTRACT: To enhance the electromagnetic transient performance and torque dynamic response quality of permanent magnet synchronous motor (PMSM) vector control systems, an improved fuzzy nonlinear active disturbance rejection control (IFNLADRC)-based dual-loop sensorless electromagnetic control method is proposed. Firstly, the nonlinear function fal_{new} is optimized to resolve the zero-point discontinuity and high-frequency chattering issues of traditional functions. A fuzzy logic controller is employed to optimize the parameters of the nonlinear state error feedback (NLSEF) control law, improving control stability. An improved extended state observer (IESO) is designed to accurately estimate the total system disturbances and achieve modular decoupling, which reduces the difficulty of parameter tuning. The controller adopts dual-loop control for comprehensive and efficient system regulation, and it integrates a linear extended state observer (LESO) with a normalized phase-locked loop (PLL) to realize high-precision sensorless estimation. Simulation results show that the proposed method outperforms traditional controllers in speed response performance, and it significantly suppresses speed fluctuations and current chattering under load disturbances. Under test conditions of speed steps ($1000\,\mathrm{r/min} \rightarrow 1300\,\mathrm{r/min} \rightarrow 1000\,\mathrm{r/min}$) and load torque steps (± 10 N), the steady-state speed error after each speed transition in sensorless control is only $\pm 0.06\,\mathrm{r/min}$ with accurate rotor position estimation, effectively improving the dynamic response, anti-disturbance performance, and control precision of the PMSM control system.

1. INTRODUCTION

In the critical stage of advancing China's "dual carbon" strategy and accelerating the digital transformation of new-type industrialization and intelligent manufacturing, permanent magnet synchronous motors (PMSMs) have become the core power executive components of high-efficiency energy-saving transmission systems and high-end intelligent equipment. Leveraging the core advantages of permanent magnet excitation coupling, efficient electromagnetic energy conversion, high-precision electromagnetic control characteristics, low harmonic loss, and high dynamic response electromagnetic torque output, PMSMs also serve as strategically fundamental electromagnetic drive equipment supporting efficient energy utilization, independent control of high-end equipment, and industrial intelligent upgrading [1–4].

Traditional PMSM vector control employs a proportional-integral (PI) control for the speed loop, which is easy to implement and adjust but suffers from shortcomings such as vulnerability to external disturbances and excessive overshoot. To improve the anti-disturbance performance of PMSM control systems, researchers have proposed various control strategies: sliding mode control [5], neural network control [6], fuzzy proportional integral differential (PID) control [7], robust control [8], and active disturbance rejection control (ADRC) [9], etc., which have been applied to PMSM system control. Han [10] innovatively proposed nonlinear active disturbance rejection control (NLADRC) technology, whose core advantage lies in achieving excellent control objectives without relying on an accurate mathematical model. Ref. [11] proposed a fuzzy PID-based control system that modifies parameters through fuzzy processing of error variables, but it requires adjusting multiple parameters and exhibits limited effectiveness under large errors. Ref. [12] presented an improved ADRC strategy that obtains an approximate tuning relationship through multiple algorithm iterations of parameter relationships; however, this method involves extensive algorithm iterations and is inconvenient for practical operation. Ref. [13] proposed an improved ADRC strategy based on a sliding mode observer; while the phase-locked loop (PLL) in sensorless control can compensate for phase delay, it requires designing complex adaptive laws or filter parameters, increasing the difficulty of engineering implementation. Ref. [14] addressed the high computational complexity and design complexity of field-oriented control systems for dual three-phase PMSMs by proposing an improved four-vector Space Vector Pulse Width Modulation (SVPWM) algorithm based on virtual voltage vectors, which simplifies calculations while retaining harmonic suppression capabilities, but fails to explore control performance under variable speed, variable load, and extreme operating conditions. Ref. [15] targeted the steady-state position estimation error of traditional PLLs in PMSM sensorless control during ramp acceleration and deceleration. It innovatively combined a sliding mode observer, a complex coefficient filter, and a frequency-locked loop (FLL),

* Corresponding author: Haifeng Zhang (3516485006@qq.com).

constructing an FLL based on the complex coefficient filter to realize adaptive adjustment of its center frequency, thereby eliminating the steady-state position estimation error in ramp speed tracking in principle. However, the study only focuses on the medium-high speed range of surface-mounted PMSMs and does not explore position estimation performance when the back electromagnetic field (EMF) is weak in the low-speed range.

To address the aforementioned issues, this paper proposes an improved fuzzy nonlinear active disturbance rejection controller (IFNLADRC). The specific methods are as follows:

1. Optimize the design of the nonlinear function fal_{new} to resolve the non-differentiability at the segmentation point, zero-point discontinuity, and high-frequency chattering of the traditional *fal* function. Simultaneously, construct a fuzzy logic controller with speed error and error change rate as inputs and the NLSEF parameter correction value as output to realize adaptive optimization of the nonlinear state error feedback control law parameters. The improved system robustness and control stability can be verified through simulations.

2. Propose an improved extended state observer (IESO). Accurate estimation of total system disturbances is achieved by constructing a disturbance error differential equation and verifying Lyapunov stability. Meanwhile, the parameter coupling relationship between the tracking term and disturbance observation term in the traditional observer is decoupled, and a unified parameter tuning formula centered on the observer bandwidth is designed. The reduced complexity of parameter tuning can be verified through transfer function derivation and practical parameter tuning processes.

3. Establish a dual-loop (speed-current) improved fuzzy nonlinear active disturbance rejection control architecture. The angular velocity and q-axis current are used as inputs to the speed loop and current loop observers, respectively, and the disturbance estimation value is incorporated into the parameter decoupling process as a compensation term to realize coordinated disturbance compensation and decoupling control of the dual loops. The suppression effect of the dual-loop architecture on speed fluctuations and current chattering under load disturbances can be verified through simulation comparisons [16].

4. Integrate LESO back EMF observation with normalized PLL technology, design a rotor position lag compensation formula to compensate for the estimation delay of LESO, and construct a sensorless detection module. Simulation verification confirms that this module achieves high-precision estimation with a steady-state speed error of ± 0.06 r/min after each speed transition and effectively eliminates the phase delay in rotor position detection.

The synergistic application of this series of improved control technologies in PMSM vector control systems enables the construction of high-precision, high-robustness motor drive control systems adaptable to multiple scenarios, such as industrial servo, new energy vehicle drives, and high-efficiency energy-saving transmissions. By optimizing the nonlinear function fal_{new} and combining it with a fuzzy logic controller for adaptive parameter optimization, the high-frequency chattering caused by zero-point discontinuity and non-differentiability at the segmentation point of traditional NLADRC functions is effectively suppressed. This significantly improves the smoothness of control signals, reduces the impact and fatigue damage of current chattering on key electrical components such as power devices and stator windings, and extends the service life and operational reliability of the motor drive system. The implementation of parameter decoupling design and unified bandwidth tuning dynamically adjusts the controller parameter tuning logic based on the motor's real-time speed, load torque, and stator current. This approach not only reduces the difficulty and trial-and-error cost of on-site parameter adjustment but also balances the dual requirements of system dynamic response speed and steady-state control precision, adapting to the complex control needs of PMSMs under variable speed and variable load conditions. The system further integrates the IESO with the dual-loop (speed-current) architecture, using angular velocity and q-axis current as inputs to the dual-loop observers to accurately estimate composite system disturbances caused by parameter perturbations, load mutations, and electromagnetic interference in real time. By incorporating the disturbance estimation value into the parameter decoupling process as a compensation term, coordinated dynamic feedforward compensation of the dual loops is achieved, greatly enhancing the system's anti-disturbance capability under severe disturbance conditions. Meanwhile, the sensorless detection module constructed by integrating LESO with a normalized PLL accurately compensates for the phase delay in back EMF estimation, eliminating the installation space constraints, maintenance costs, and failure risks associated with mechanical position sensors, and improving the structural simplicity and environmental adaptability of the drive system.

2. MATHEMATICAL MODEL OF PERMANENT MAGNET SYNCHRONOUS MOTOR

For the rotor structure of a surface-mounted PMSM, under ideal conditions, vector control is realized through coordinate transformation. Based on the field-oriented control principle [17], the voltage equations in the synchronous rotating d-q frame are derived as follows:

$$\begin{cases} u_d = Ri_d + L_s \frac{d}{dt} i_d - \omega_e L_s i_q \\ u_q = Ri_q + L_s \frac{d}{dt} i_d + \omega_e \left(L_s i_d + \psi_f \right) \end{cases} \tag{1}$$

where u_d and u_q are the stator d-axis and q-axis voltage components; i_d and i_q are the stator d-axis and q-axis current components; R is the stator resistance; L_s is the stator inductance; ψ_f is the permanent magnet flux linkage; ω_e is the electrical angular velocity. The motion equation of the surface-mounted PMSM is:

$$\frac{\mathrm{d}\omega_m}{\mathrm{d}t} = \frac{T_e}{J} - \frac{T_L}{J} - \frac{B\omega_m}{J} \tag{2}$$

where T_e is the electromagnetic torque; B is the damping coefficient; T_L is the load torque; J is the moment of inertia.

Due to motor parameter variations and modeling uncertainties, the PMSM model can be expressed as:

$$\begin{cases} u_d = Ri_d + L_s \frac{d}{dt} i_d - \omega_e L_s i_q + \Delta u_d \\ u_q = Ri_q + L_s \frac{d}{dt} i_d + \omega_e L_s i_q + \omega_e \psi_f + \Delta u_q \\ T_e = \frac{3}{2} p_n \psi_f i_q + \Delta T_e \end{cases} \tag{3}$$

where Δu_q, Δu_d, and ΔT_e are uncertain disturbances caused by parameter perturbations inside the PMSM.

3. DESIGN OF A ANTI-NOISE CONTROLLER FOR SPEED AND CURRENT LOOPS

3.1. Improving the Design of Nonlinear Self-Disturbance-Immune Controller

In the PMSM field-oriented control (FOC) framework, the outer speed loop faces severe challenges to system robustness when dealing with large speed difference fluctuations, measurement noise, and load-side electromagnetic disturbances. Speed deviations caused by load mutations are amplified by the speed regulator and directly propagated to the inner q-axis current loop, leading to drastic fluctuations in electromagnetic torque commands and thus undermining the dynamic stability of the system. Therefore, designing a high-performance nonlinear active disturbance rejection controller is particularly crucial.

The structure of traditional NLADRC [18] consists of a Tracking Differentiator (TD), a Nonlinear State Error Feedback (NLSEF) control law, and a Nonlinear Extended State Observer (NESO). In this paper, a first-order NLADRC is designed based on the motor mechanical motion equation.

The design of the nonlinear tracking differentiator breaks the limitations of traditional linear differentiators. Its nonlinear structure achieves high-precision tracking and differential extraction of input signals, while exhibiting strong anti-noise capability and optimized dynamic performance. The discrete form of the tracking differentiator is as follows:

$$\begin{cases} f_h = \mathcal{F}han\left(\omega_{ref}(t) - \omega_m^*, \dot{\omega}_{ref}(t), r_0, h_0\right), \\ \omega_{ref}(t+h) = \omega_{ref}(t) + h\dot{\omega}_{ref}(t), \\ \dot{\omega}_{ref}(t+h) = \dot{\omega}_{ref}(t) + h f_h \end{cases} \tag{4}$$

where f_h is the intermediate variable of the tracking differentiator; *fhan* is the fastest synthesis function; ω_m^*, ω_{ref}, $\dot{\omega}_{ref}$ are the given reference angular velocity, the actual angular velocity after transition, and its differential value; h is the sampling step; h_0 is the filtering factor; r_0 is the speed factor.

The nonlinear parts of the traditional NESO and NLSEF are composed of the nonlinear function *fal*, whose expression is *fal*, expressed as:

$$fal(e, \alpha, \delta) = \begin{cases} e/\delta^{(1-\alpha)}, & |e| \le \delta \\ \text{sign}(e)|e|^{\alpha}, & |e| > \delta \end{cases} \tag{5}$$

where α is the speed tracking factor related to the function *fal*; α is the filtering factor. As can be seen from the equation, the function *fal* is non-differentiable at the linear-nonlinear segmentation point δ, making it highly sensitive to the actual value of the error. If δ is too small, the severe high-frequency chattering of the function *fal* will occur, thereby reducing system robustness.

Improve the nonlinear function fal_{new} as follows:

$$fal_{new} = \begin{cases} k_1 \sin(e) + k_2 e + k_3 \tan(e), & |e| < \delta \\ \text{sign}(e)|e|^{\alpha}, & |e| > \delta \end{cases} \tag{6}$$

Through continuous solution at the segmentation point, the following is obtained:

$$\begin{cases} k_1 = \frac{\alpha\delta^{\alpha-1}\tan(\delta+\delta^3) - \delta^{\alpha}}{\tan(\delta+\delta^3) - \sin(\delta)} \\ k_2 = 0 \\ k_3 = \frac{(1+\delta^2)\left(\delta^{\alpha}\cos(\delta) - \alpha\delta^{\alpha-1}\sin(\delta)\right)}{\cos(\delta+\delta^3)\tan(\delta) - \sin(\delta)} \end{cases} \tag{7}$$

The *fal* function possesses a constant derivative and a fixed gain for minor noises and errors. Consequently, noises are linearly amplified without abrupt mutations, while the amplification factor remains constant. The derivative of the fal_{new} function approaches zero at $e = 0$, and its gain for extremely small noise and error perturbations near the zero point is considerably lower than that of the *fal* function, which effectively suppresses minor disturbances near the zero point. The superiority of fal_{new} does not lie in stronger robustness over the entire interval, but in precise optimization for its design objective, namely the suppression of minor error noises near the zero point. This also constitutes the core application scenario of *fal*-type functions in ADRC, i.e., error handling near the zero point in extended state observers and error feedback control as illustrated in Fig. 1.

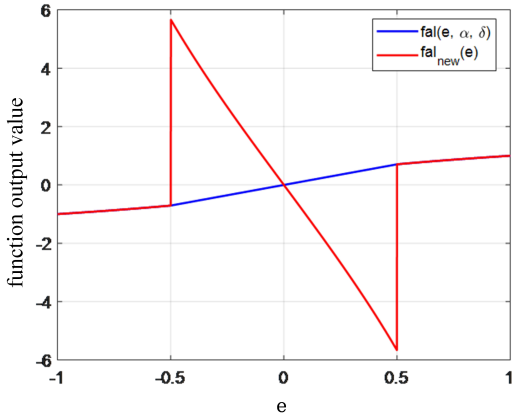

FIGURE 1. Comparison of variation characteristics between *fal* and fal_{new} functions.

The value of the relevant coefficient k_0 of the NLSEF control law is undetermined and thus can be determined through the selection of membership functions and fuzzy rules. Specifically, the error e between the given speed and the estimated feedback speed from the state observer and the error change rate ec are set as the two input terminals of the fuzzy logic controller, and the correction value Δk of the parameter to be tuned in the error

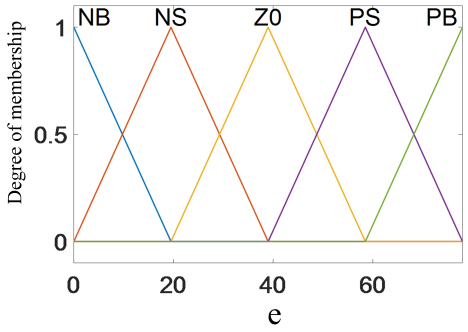

FIGURE 2. Triangular fuzzy membership function of error e.

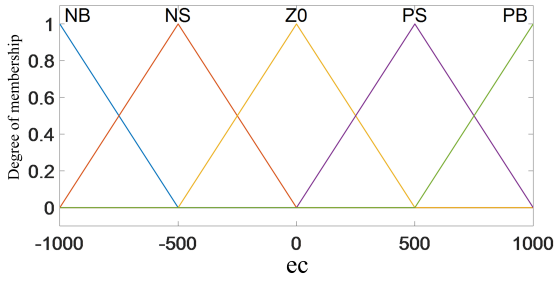

FIGURE 3. Triangular fuzzy membership functions of the error change rate ec.

state feedback is set as the output of the fuzzy controller. The obtained correction value Δk is incorporated into $k = k_0 + \Delta k$ through fuzzification, where k_0 is the initial compensation coefficient. Triangular fuzzy sets are selected as the membership functions, and the upper and lower boundary points are reasonably set according to the region to be fuzzified, as shown in Figs. 2–5. The fuzzy rules are shown in Table 1.

TABLE 1. Fuzzy control rules.

$ec \setminus e$	NB	NS	Z0	PS	PB
NB	Z0	Z0	Z0	NS	NB
NS	Z0	Z0	NS	NS	NB
Z0	PS	PS	PS	PB	PB
PS	Z0	Z0	PS	PS	PB
PB	Z0	Z0	Z0	PS	PB

Figure 5 shows the corresponding three-dimensional output surface diagram of the fuzzy controller.

3.2. Improved Design of the Extended State Observer

The design objective of the improved extended state observer is to achieve more accurate estimation of total system disturbances. Parameter decoupling aims to resolve the mutual coupling between the observer module and the tracking module, reducing the difficulty of parameter tuning.

The model can be designed based on known quantities:

$$\frac{d\omega_m}{dt} = \frac{T_e}{J} - \frac{T_L}{J} - \frac{B\omega_m}{J} = b_0 u + f \tag{8}$$

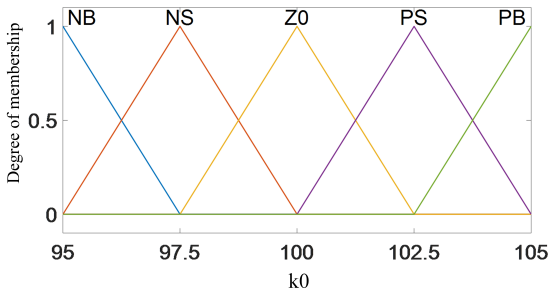

FIGURE 4. Triangular fuzzy membership function of parameter k_0.

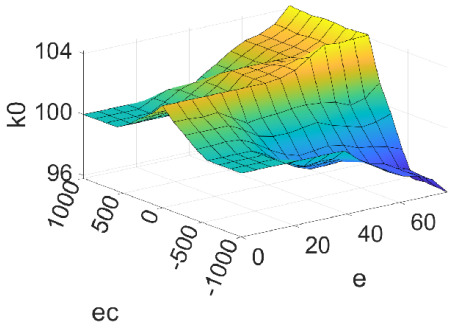

FIGURE 5. Three-dimensional output surface plot of the fuzzy controller.

$$\dot{\hat{f}} = -C(\hat{f} - f) = -C\hat{f} + C(\omega_m - b_0 u) \tag{9}$$

The disturbance experienced by the speed loop of the PMSM system is expressed as Eq. (8): $f = -\frac{T_L}{J} - \frac{B\omega_m}{J} + (b - b_0)u$, where $b = \frac{3n_p\psi_f}{2J}$ is the actual gain of the controller; $u = i_q$ is the final output of the controller; b_0 is the estimated value of b; $\hat{f}$ is the estimated value of the actual disturbance; C is the gain of disturbance estimation.

Since the control principle of the current loop is consistent with that of the speed loop, the disturbance experienced by the current loop can be represented using the same variables as the speed loop. From Eq. (3), the q-axis current equation is derived as:

$$\frac{di_q}{dt} = \frac{1}{L_q}u_q - \frac{R}{L_q}i_q - \frac{\omega_e}{L_q}(L_d i_q + \psi_f) \tag{10}$$

From Eq. (10), we can set $x_1 = i_q$, $x_2 = f = -b_0(u_q^* - u_q) - \frac{Ri_q}{L_q} - \frac{\omega_e(L_d i_d + \psi_f)}{L_q}$, where f represents the total disturbance arising from complex unknown factors, such as concentrated $\frac{\omega_e\psi_f}{L_q}$ variations, perturbations of the parameters resistor R and inductor L_q and external disturbances.

A corresponding differential equation for the disturbance error is established, and the intermediate variable $z = \hat{f} - C\omega m$ is introduced. By differentiating and combining, the following is obtained:

$$\begin{cases} e_d = \hat{f} - f \\ \dot{e}_d + Ce_d = 0 \\ \dot{z} = \dot{\hat{f}} - C\dot{\omega}_m \end{cases} \tag{11}$$

The observer expression is solved as:

$$\begin{cases} \dot{z} = -C\hat{f} - Cb_0u = -C\left(z + C\omega_m\right) - Cb_0u \\ \hat{f} = z + C\omega_m \end{cases} \tag{12}$$

To verify whether the perturbation error differential equation in (11) satisfies the Lyapunov stability condition, transform it and substitute the transformed e_d into the Lyapunov equation:

$$\begin{cases} \dot{e}_d = -C\left(\hat{f} - f\right) \\ V = e_d^2 \end{cases} \tag{13}$$

The solution is:

$$\dot{V} = 2e_d\dot{e}_d = -2Ce_d^2 = -2C\left(\hat{f} - f\right)^2 \tag{14}$$

When $h > 0$, $\dot{V} < 0$ is satisfied, fulfilling the Lyapunov stability condition, thus enabling accurate estimation of disturbance quantities.

Further analysis of the coupling problem reveals that designing a parameter-decoupled extended state observer can effectively reduce the difficulty of controller parameter tuning. By removing the *fal* function from the traditional extended state observer and applying a Laplace transform, the relationships between the system input b_0u, output ω_m, and state variables are obtained:

$$\begin{cases} z_{11} = \frac{s}{s(s+\beta_1)+\beta_2}\, b_0u + \frac{\beta_1 s+\beta_2}{s(s+\beta_1)+\beta_2}\, \omega_m \\ z_{12} = \frac{\beta_2}{s(s+\beta_1)+\beta_2}\, b_0u + \frac{\beta_2 s}{s(s+\beta_1)+\beta_2}\, \omega_m \end{cases} \tag{15}$$

The NLSEF control law is designed as:

$$\begin{cases} u_0 \equiv K_p fal(e_1, \alpha_1, \delta_1) \\ u = \frac{u_0 - (z_{12}+z_{22})}{b_0} \end{cases} \tag{16}$$

Combining Eq. (15) (with the *fal* function removed) and Eq. (16), the value of u is obtained. The controlled object is defined as:

$$u = \frac{1}{b_0}\frac{s^2+\beta_1 s+\beta_2}{s^2+\beta_1 s+k_p s}\left(k_p\omega_m^* - \frac{(k_p\beta_1+\beta_2)s+k_p\beta_2}{s^2+\beta_1 s+\beta_2}\,\omega_m\right) \tag{17}$$

Control objects can be set:

$$y = \frac{1}{s}\left(f + b_0u\right) \tag{18}$$

The closed-loop transfer function of a first-order closed-loop system can be obtained by combining Eqs. (17) and (18):

$$\begin{aligned} Y(s) &= G_r(s)V(s) + G_f(s)F(s) \\ &= \frac{k_p}{s+k_p}V(s) + \frac{s^2+\beta_1 s+k_p s}{(s+k_p)(s^2+\beta_1 s+\beta_2)}F(s) \end{aligned} \tag{19}$$

where $G_r(s)$ is the system tracking transfer function; $G_f(s)$ is the system disturbance transfer function. k_p determines the system's tracking performance, while the system's disturbance rejection capability depends on k_p, β_1, and β_2. An interactive coupling relationship exists between the system's tracking term and disturbance observation term, increasing the difficulty of controller parameter tuning.

Integrating the aforementioned total system disturbance estimation and observer parameter decoupling process, a new improved extended state observer is designed:

$$\begin{cases} e_1 = \omega_m - z_{21} \\ \dot{z}_{21} = z_{22} + b_0u + \hat{f} \\ \dot{z}_{22} = \beta_1 fal_{new}\frac{d}{dt}e_1 + \beta_2 fal_{new}e_1 \end{cases} \tag{20}$$

$$\begin{cases} e_2 = \omega_m^* - z_{21} \\ u_0 = k_0e_2 \\ u = \frac{u_0 - \left(z_{22}+\hat{f}\right)}{b_0} \end{cases} \tag{21}$$

where $\hat{f}$ is the disturbance compensation; z_{22} is used to track the residual disturbance in the PMSM system excluding $\hat{f}$; u is the final output of the control system for regulating the speed loop and current loop; parameter tuning of the ADRC system adopts the bandwidth tuning method:

$$\begin{cases} \beta_1 = 2\omega_0 \\ \beta_2 = \omega_0^2 \end{cases} \tag{22}$$

In Eq. (22), ω_0 represents the bandwidth of the improved extended state observer.

The principal block diagram of the improved fuzzy nonlinear active disturbance rejection controller is shown in Fig. 6, where the dashed block represents the improved extended state observer.

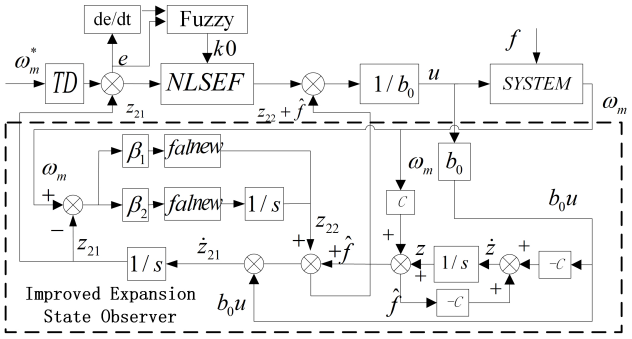

FIGURE 6. Principle block diagram of the improved fuzzy nonlinear active disturbance rejection controller.

4. SENSORLESS DESIGN

Traditional mechanical contact sensors require additional installation space, increasing the overall volume of the motors. Sensorless designs eliminate physical detection components, resulting in simpler structures, wear-free, maintenance-free operation, lower costs, reduced failure rates, faster response

speeds, and more flexible installation. This paper employs LESO to observe back EMF. The expression is as follows:

$$\begin{cases} E_\alpha = z_{31} - i_\alpha \\ \dot{z}_{31} = z_{41} - \beta_3 E_\alpha + b_0 u + f_1 \\ \dot{z}_{41} = -\beta_4 E_\alpha \end{cases} \tag{23}$$

$$\begin{cases} E_\beta = z_{32} - i_\beta \\ \dot{z}_{32} = z_{42} - \beta_3 E_\beta + b_0 u + f_2 \\ \dot{z}_{42} = -\beta_4 E_\beta \end{cases} \tag{24}$$

In Eqs. (23) and (24): z_{31} and z_{32} represent the observed current values on the α-β axis, while $f_1 + z_{41}$, $f_2 + z_{42}$ denote the estimated total disturbance values on the α-β axis, where $f_1 = -\frac{R_s i_\alpha}{L_s}$ and $f_2 = -\frac{R_s i_\beta}{L_s}$, and the estimated back-EMFs $\hat{E}_\alpha$ $\hat{E}_\beta$ on the α-β axis can be extracted from z_{41} and z_{42}, respectively, as follows:

$$\begin{cases} \hat{E}_\alpha = -L_s z_{41} \\ \hat{E}_\beta = -L_s z_{42} \end{cases} \tag{25}$$

A normalized phase-locked loop structure is employed to extract rotor information from the PMSM, enhancing the accuracy of rotational speed and rotor position. To compensate for the delay caused by the LESO estimation back-EMF, rotor position compensation is required. The position compensation formula is as follows:

$$\theta_{\text{lag}} = 2 \arctan\left(\frac{\omega_e}{\omega_0}\right) \tag{26}$$

In Eq. (26), θ_{lag} represents the lag compensation angle value, and ω_e denotes the estimated electrical angle. The structure block diagram of the normalized PLL is shown in Fig. 7.

5. SIMULATION EXPERIMENT VALIDATION

To verify the feasibility and effectiveness of the proposed IFNLADRC in suppressing the anti-disturbance control performance of the PMSM dual-loop control system under speed mutations and load mutations, a simulation model of PMSM vector control based on IFNLADRC was established and implemented using MATLAB/Simulink. Fig. 8 shows the block diagram of the sensorless vector control for PMSM with model-compensated nonlinear active disturbance rejection. The specific simulation parameters of the PMSM are listed in Table 2.

TABLE 2. Motor parameters.

Parameters	Parameter value
Stator Inductance L_s/mH	8.5
Stator resistance R/Ω	2.875
Magnetic chain ψ_f/Wb	0.175
Pole pairs P	4
Moment of inertia J/(kg·m^2)	0.003
Damping coefficient B	0.008
DC voltage U_{dc}/V	311

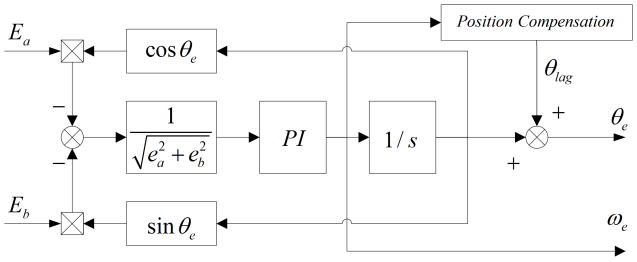

FIGURE 7. Structure block diagram of the normalized phase-locked loop.

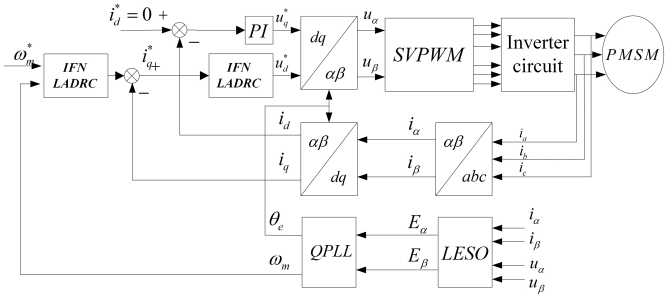

FIGURE 8. Block diagram of sensorless vector control for PMSM based on IFNLADRC.

To further validate the control performance of the improved IFNLADRC under various conditions, this paper conducts comparative experiments in sensorless control scenarios using traditional PI controllers, LADRC, NLADRC, Multi-stage ADRC (referring to a cascaded ADRC structure with dual extended state observers), and the proposed IFNLADRC. For the system speed loop: PI parameters: $kp = 0.3$, $ki = 5$; LADRC parameters: $kp = 100$, $\omega_0 = 300$; NLADRC parameters: $kp = 100$, $\omega_0 = 300$; Multi-stage ADRC parameters: $kp = 100$, $\beta_{11} = 30$, $\beta_{12} = 225$, $\beta_{21} = 1200$, $\beta_{22} = 360000$; IFNLADRC parameters: $kp = 100$, $\beta_{11} = 30$, $\beta_{12} = 225$, $\beta_{21} = 1200$, $\beta_{22} = 360000$; Current loop PI parameters: $kp = 45$, $ki = 220$.

The speed response performance of each controller under sensorless control was verified under the following conditions: initial start-up at 1000 r/min, speed transition to 1300 r/min with a sudden load reduction of 10 N at 0.2 s, and speed reduction to 1000 r/min with a sudden load increase of 10 N at 0.4 s. The speed curves under the above conditions are shown in Fig. 9.

As can be seen from Fig. 9, the proposed IFNLADRC method exhibits a fast dynamic response and excellent anti-disturbance capability; after loading or unloading, it can quickly recover to the reference speed, suppress speed fluctuations, and reduce the chattering amplitude of the system, and reduce the system chattering amplitude. The speed overshoot, rise time ratio, and adjustment time of the IFNLADRC control method and other control methods in the three stages are listed in Table 3.

Figures 10 and 11 show the response curves of the q-axis current i_q and electromagnetic torque after start-up, respectively, with high curve similarity. Analysis indicates that the q-axis current i_q rapidly reaches its maximum value in the initial start-

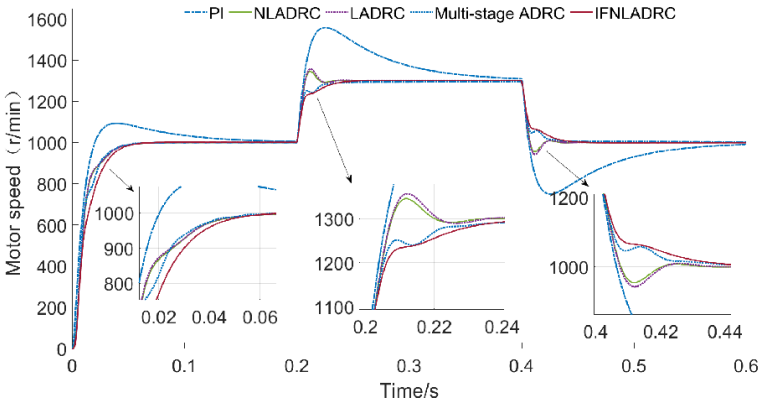

FIGURE 9. Motor speed response curves under various controllers.

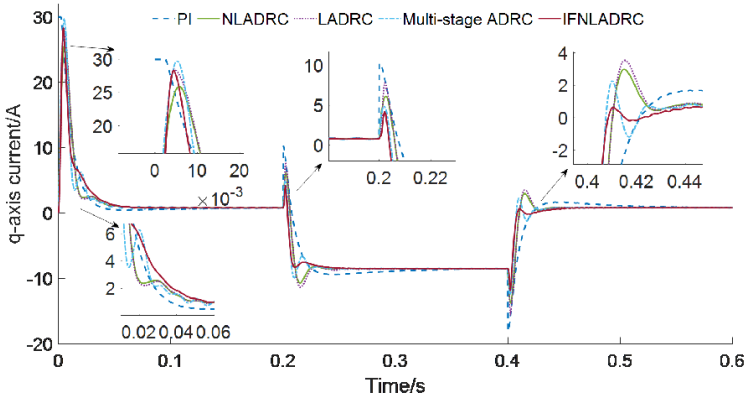

FIGURE 10. q-axis current response curves under each controller.

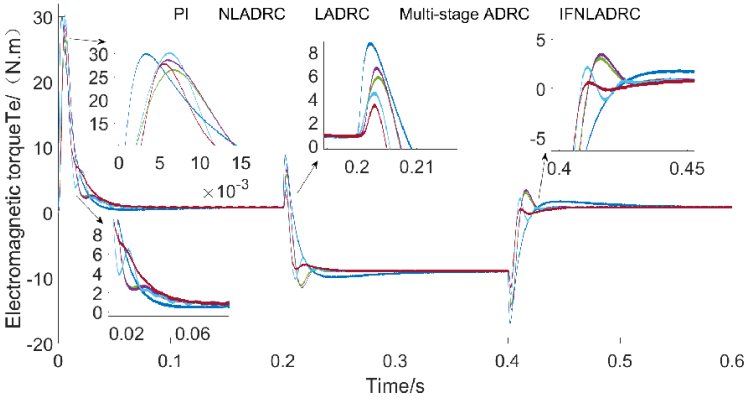

FIGURE 11. Electromagnetic torque response curves under each controller.

up stage. The speed drop of the IFNLADRC control method after loading at 0.2 s is 87.30%, 90.58%, 91.62%, and 86.33% of those of the multi-stage ADRC, NLADRC, LADRC, and PI controllers, respectively. A smaller start-up current reduces the cost requirements for hardware equipment. Additionally, current fluctuations are further suppressed after start-up during loading and unloading. Meanwhile, compared with other controllers, IFNLADRC outputs more stable torque. Therefore, the proposed IFNLADRC control method also exhibits excellent performance during start-up.

The LESO designed in this paper achieves a precise estimation of the error between the observed PMSM speed and the actual speed. The bandwidth ω_0 of the LESO is set to 6000, and the time interval is set to 0.05–0.06 s. The comparison results are shown in Fig. 12. After normalization, the back EMF observed by the designed LESO exhibits a small error with the ro-

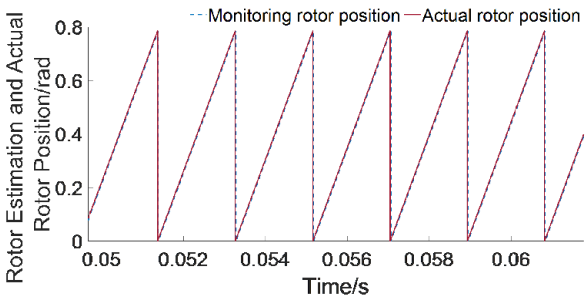

FIGURE 12. LESO actual rotor position and estimated rotor position waveform.

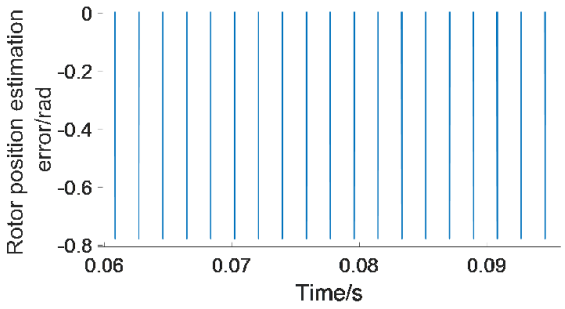

FIGURE 14. Sensorless rotor position estimation error waveform.

TABLE 3. Performance comparison of different control methods.

Control method	Overshoot (%)	Rise time (s)	Regulation time (s)
Stage 1 (0→1000 r/min)			
PI	10.2	0.02	0.115
NLADRC	1.1	0.03	0.006
LADRC	2.6	0.03	0.005
Multi-stage ADRC	3.3	0.035	0.006
IFNLADRC	0	0.05	0.008
Stage 2 (1000→1300 r/min)			
PI	20.8	0.008	0.315
NLADRC	4.6	0.010	0.223
LADRC	5.4	0.011	0.220
Multi-stage ADRC	0.8	0.012	0.221
IFNLADRC	0	0.015	0.230
Stage 3 (1300→1000 r/min)			
PI	25.3	0.03	0.551
NLADRC	5.1	0.02	0.430
LADRC	6.0	0.02	0.430
Multi-stage ADRC	4.3	0.02	0.430
IFNLADRC	3.0	0.01	0.420

tor position angle extracted by the rotor position-compensated quadrature PLL. As shown in Fig. 13, the steady-state speed fluctuation estimated by the LESO is within $\pm 0.06\,\mathrm{r/min}$, indicating low chattering and high precision of the method. As shown in Fig. 14, the sensorless control can accurately estimate the rotor position, reducing the steady-state error during tracking and avoiding the phase delay problem.

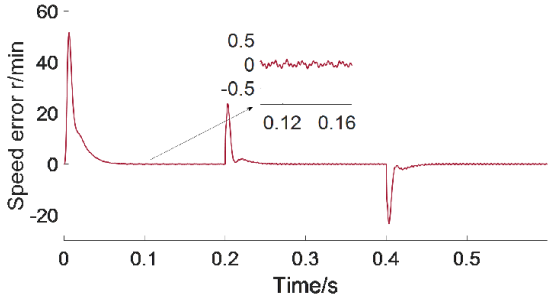

FIGURE 13. LESO estimated speed error waveform.

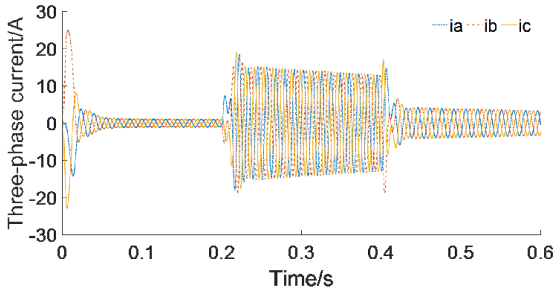

FIGURE 15. Three-phase current waveform under NLADRC control.

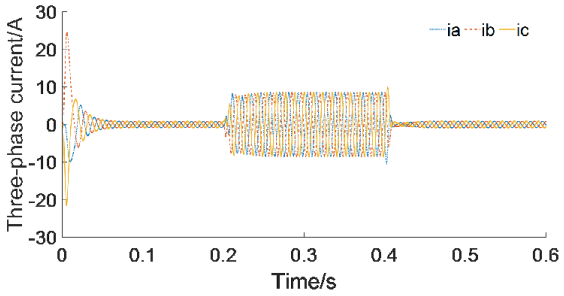

FIGURE 16. Three-phase current waveform under IFNLADRC control.

A comparison between Figs. 15 and 16 shows that compared with the traditional NLADRC control method, the IFNLADRC control method achieves more stable three-phase currents i_a, i_b, and i_c of the PMSM. Therefore, the improved IFNLADRC control method enhances the stability of the controller to a certain extent.

6. CONCLUSION

This paper focuses on enhancing the electromagnetic transient performance and torque dynamic response quality of PMSM vector control systems. To achieve this goal, an IFNLADRC-based motor vector control method is proposed. The improved nonlinear function fal_{new} for NLADRC resolves the discontinuity problem of traditional nonlinear functions and thus enhances the anti-disturbance performance. Meanwhile, a fuzzy logic controller is designed to optimize the NLSEF parameters, which achieves more stable control performance. The designed improved extended state observer can accurately estimate the residual system disturbances, which not only reduces the difficulty of parameter tuning but also improves the tracking per-

formance and anti-disturbance capability of the control system. Simulation results demonstrate that the proposed control strategy improves the response speed of the speed regulation system and reduces the steady-state error. Additionally, the design of the LESO-based sensorless control combined with a quadrature PLL limits the steady-state speed error after each speed transition during simulation to ± 0.06 r/min, enabling the accurate detection of the rotor position and ensuring the stability of q-axis current and electromagnetic torque output. There remains room for further research on parameter adjustment in the active disturbance rejection control loop; future work will consider integrating algorithm-based parameter optimization.

ACKNOWLEDGEMENT

National Natural Science Foundation of China (No. 52067008); Key Research and Development Program of Ganzhou (No. GZ2024ZDZ006).

REFERENCES

[1] Wang, B. W., "Analysis on energy efficiency improvement and emission reduction strategies in new material production workshop," *Papermaking Equipment & Materials*, Vol. 54, No. 8, 115–117, 2025.

[2] Chen, W. J. and H. Luo, "Design and research of motors for new energy vehicle," *Mechanical and Electrical Information*, Vol. 54, No. 12, 17–20, 2025.

[3] Lian, X. L. and W. L. Si, "Lightweight design and efficiency improvement path analysis of permanent magnet synchronous motors for new energy vehicles," *Automotive Test Report*, Vol. 2025, No. 21, 34–36, 2025.

[4] Wang, D. M., S. Y. Li, and Y. P. Liang, "Comprehensive review of thermal design and thermal management technologies for new energy vehicle drive motors," *Transactions of China Electrotechnical Society*, Vol. 41, No. 2, 389–415, 2026.

[5] Guo, Z. Q., C. C. Gao, and Y. D. Jiang, "Design of servo control system for permanent magnet synchronous motor of electric vehicles based on sliding mode control algorithm," *Automation & Instrumentation*, Vol. 47, No. 8, 17–21, 2015.

[6] Li, X. W., "Fault diagnosis method for inter-turn short circuit of permanent magnet synchronous motors based on RBF neural network," *Technology Innovation and Application*, Vol. 15, No. 14, 26–30, 2025.

[7] Huang, M. Y., "Research on self disturbance rejection control of permanent magnet synchronous motor based on smith-fuzzy PID," *Electronic Design Engineering*, Vol. 33, No. 12, 36–39, 2025.

[8] Qi, X., J. J. Xu, X. M. Zhou, *et al.*, "Low switching frequency predictive control of permanent magnet synchronous motors with strong robustness," *Journal of Tianjin University*, Vol. 58, No. 8, 865–873, 2025.

[9] Yuan, H. R., F. Q. Zhou, and J. H. Sun, "Improved linear active disturbance rejection control of PMSM based on load torque observation," *Electronic Measurement Technology*, Vol. 48, No. 9, 36–43, 2025.

[10] Han, J. Q., "Auto disturbances rejection control technique," *Frontier Science*, Vol. 1, No. 1, 24–31, 2007.

[11] Hou, J. R. and C. W. Li, "Speed control of energy-saving permanent magnet synchronous motor for metro based on fuzzy PID," *Ordnance Industry Automation*, Vol. 44, No. 1, 33–37, 2025.

[12] Song, H., P. Yuan, and Y. J. Zhang, "ARDC speed regulation strategy of nuclear main pump permanent magnet synchronous motor based on improved butterfly optimization algorithm," *Nuclear Electronics & Detection Technology*, Vol. 43, No. 2, 221–228, 2023.

[13] Li, B. B., Y. Zhao, A. Gao, *et al.*, "Active disturbance rejection control of PMSM based on improved exponential convergence law sliding mode observer," *Modular Machine Tool & Automatic Manufacturing Technique*, Vol. 47, No. 8, 107–111, 2025.

[14] Li, C. N., X. Guan, Z. Y. Yu, *et al.*, "Research on field orientation control strategy based on virtual voltage vector," *Electric Machines & Control Application*, Vol. 50, No. 12, 66–73, 2023.

[15] Zhang, R. J., Q. F. Hu, J. T. Gu, *et al.*, "Position estimation error suppression of PMSM based on frequency-locked loop feedforward," *Power Electronics*, Vol. 57, No. 7, 40–43, 2023.

[16] Ren, Z. B., R. H. Huang, Y. Wu, *et al.*, "Harmonic current suppression of pmsm with quasi-resonant controller based on dual-ring adrc," *Modular Machine Tool & Automatic Manufacturing Technique*, Vol. 47, No. 3, 94–98, 2025.

[17] Wen, H. T. and X. D. Yao, "Vector control design of permanent magnet synchronous motor based on double sliding mode," *Electrical Automation*, Vol. 47, No. 5, 73–77, 2025.

[18] Li, J., X. H. Qi, Y. Q. Xia, and Z. Q. Gao, "On linear/nonlinear active disturbance rejection switching control," *Acta Automatica Sinica*, Vol. 42, No. 2, 202–212, 2016.